ACS NANO

www.acsnano.org

Article

Skin-Interfaced Superhydrophobic Insensible Sweat Sensors for Evaluating Body Thermoregulation and Skin Barrier Functions

Yangchengyi Liu, Xiaofeng Li, Hanlin Yang, Ping Zhang, Peihe Wang, Yi Sun, Fengzhen Yang, Weiyi Liu, Yujing Li, Yao Tian, Shun Qian, Shangda Chen, Huanyu Cheng,* and Xiufeng Wang*

Cite This: *ACS Nano* 2023, 17, 5588−5599

Read Online

ACCESS | Metrics & More | Article Recommendations | * Supporting Information

ABSTRACT: Monitoring sweat rate is vital for estimating sweat loss and accurately measuring biomarkers of interest. Although various optical or electrical sensors have been developed to monitor the sensible sweat rate, the quantification of the insensible sweat rate that is directly related to body thermoregulation and skin barrier functions still remains a challenge. This work introduces a superhydrophobic sweat sensor based on a polyacrylate sodium/MXene composite sandwiched between two superhydrophobic textile layers to continuously measure sweat vapor from insensible sweat with high sensitivity and rapid response. The superhydrophobic textile on a holey thin substrate with reduced stiffness and excellent breathability allows the permeation of sweat vapor, while preventing the sensor from being affected by the external water droplets and internal sensible sweat. Integrating the insensible sweat sensor with a flexible wireless communication and powering module further yields a standalone sensing system to continuously monitor insensible sweat rates at different body locations for diverse application scenarios. Proof-of-concept demonstrations on human subjects showcase the feasibility to continuously evaluate the body's thermoregulation and skin barrier functions for the assessment of thermal comfort, disease conditions, and nervous system activity. The results presented in this work also provide a low-cost device platform to detect other health-relevant biomarkers in the sweat (vapor) as the next-generation sweat sensor for smart healthcare and personalized medicine.

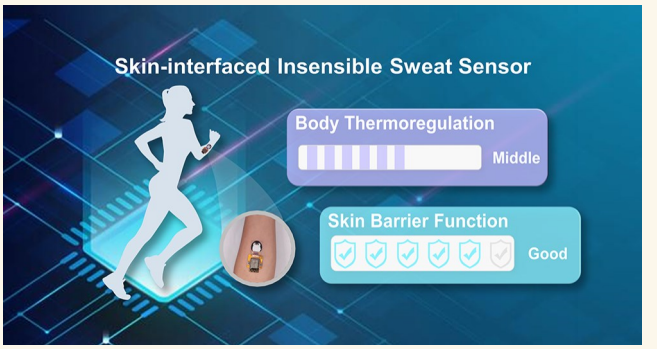

KEYWORDS: *MXene-sodium polyacrylate composites, superhydrophobic insensible sweat sensor, humidity and moisture monitoring, body thermoregulation, skin barrier functions*

1. INTRODUCTION

Stable core temperature homeostasis is essential for regulating metabolic rates and functions of the major organ systems.[1] Key in the thermoregulation process, sweating with a large specific heat capacity can absorb and transfer body heat to the surrounding environment[2,3] by evaporative cooling[4−6] when the core body temperature exceeds the hyperthermic threshold. Compared with the sensible (liquid) sweat from the sweat glands during intensive activities/exercise, insensible (vapor) sweat is secreted through the skin at a much smaller rate under mild conditions (e.g., resting or low-intensity exercise).[7,8] Although skin-interfaced microfluidic devices with colorimetric or electrical components have been developed to detect sweat rate and loss,[9−11] they are limited to working with sensible sweat only and are not suitable for the insensible sweat in a vapor state.[12,13] Besides informing on the body's thermoregulation status, the insensible sweat rate and loss can also help evaluate the skin barrier functions and nervous system activity.[14,15] The skin barrier function prevents excessive water evaporation to keep the skin hydrated.[16−18] Affected by emotional stimuli from the activities of sympathetic excitation,[19] the insensible sweat can also be used to reflect underlying health status (e.g., chronic psychological stress, anxiety, or pain).[20] Therefore, monitoring of the insensible sweat is of high interest to evaluate skin health, disease conditions (e.g., atopic dermatitis and wound healing),

Received: November 11, 2022
Accepted: February 1, 2023
Published: February 6, 2023

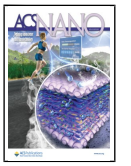

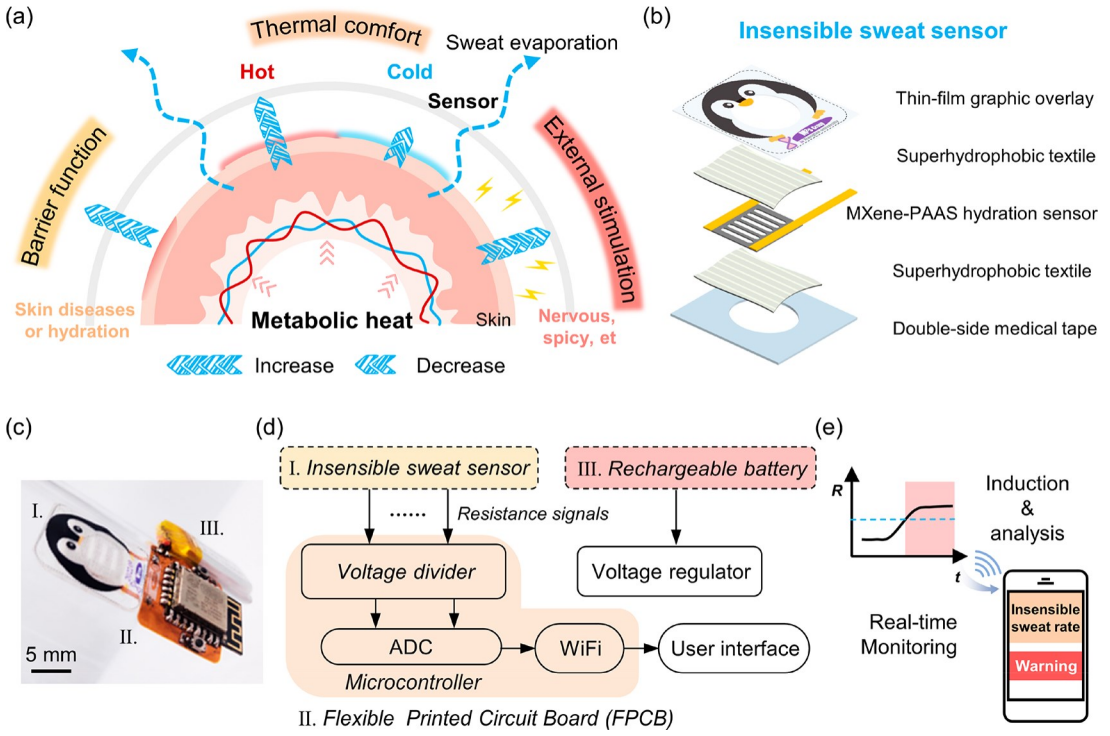

Figure 1. Design and application of the wearable insensible sweat sensing device to wirelessly monitor insensible sweat. (a) Schematic showing the applications of the insensible sweat sensor to evaluate the skin-barrier function, human thermal comfort, and emotional/gustatory stimulations. (b) Exploded view of the sensing component and (c) optical image of the integrated sensing device consisting of the (I) sensing composite, (II) FPCB, and (III) battery. (d) System-level block diagram showing signal processing and wireless transmission to the user graphic interface. (e) Schematic showing the real-time insensible sweat monitoring and analysis with a smartphone.

and emotional or gustatory stimulation (e.g., psychological stress, anxiety, and pain).[7]

Monitoring of insensible sweat can be achieved using a humidity sensor to measure the change in relative humidity caused by insensible sweat evaporation. Representative examples include a series of works that combine a closed chamber with a commercial humidity sensor to detect the moisture collected from the skin during a given period of time.[6,21−23] However, the need to separate the device from the skin for ventilating the chamber after each test makes it challenging for continuous monitoring. The bulky and stiff equipment is also not suitable for long-term wearable use.[24−26] To address these challenges, efforts have been devoted to developing a flexible humidity sensor with open chambers.[27−32] Representative examples include a honeycomb-like MoS_2 nanotube array on perforated Ecoflex,[31] sputtered Au on PVA nanomesh,[27] and MXene/silver nanowires on a silk textile.[33] However, these humidity sensors only measure skin humidity (not accurate for insensible sweat assessment), and they are also susceptible to sensible sweat and external water (droplets or moisture) to cause irreversible changes in conductive materials.[34] On the other hand, insensible sweat sensing critically relies on the design of humidity sensors to detect moisture with a fast and large response. With high conductivity, good hydrophilicity, and abundant surface terminal groups (e.g., −F and −OH), MXene has been widely adopted as a humidity-sensing material.[35] Introducing water-sensitive polymers such as poly(diallyldimethylammonium chloride) (PDAC),[36] chitosan-quercetin,[37] or bacterial cellulose[38] between the MXene layers further increases the sensitivity. However, the resulting sensor still cannot provide a large response and long-term stability. Therefore, it is highly desirable to develop high-performance wearable insensible sweat sensors for continuous monitoring in all weather conditions.

This work introduces a polyacrylate sodium (PAAS)/MXene composite on a holey polyethylene terephthalate (PET) substrate sandwiched between two superhydrophobic textile layers to yield a holey insensible sweat sensor with high sensitivity and excellent breathability (Figure 1a). The low-cost PAAS introduced between the MXene layers could significantly swell after absorbing moisture due to repulsion between carboxylate anions ($-COO^-$), increasing the sensitivity to moisture by 8 times. The holey design provides the sensor with high water permeability (96.87 g/m^2/h) and reduced stiffness for eficient detection of the insensible sweat under bending and twisting. Thanks to the superhydrophobic textile, the sensor performance is not affected by inside sensible sweat or outside water for use in all weather conditions. Integrated with a flexible electronic circuit board for signal transduction, processing, and transmission, the sensing device can wirelessly detect the insensible sweat at different body parts in real time. The capabilities of the resulting sensing device have been demonstrated for the evaluation of thermoregulation and skin barrier functions, emotional health assessment, disease diagnosis, and monitoring of emotional or gustatory stimulations. Considering the rich molecular-level information from biochemical markers (e.g., metabolites and electrolytes) in sweat, the wireless sweat sensing platform also provides opportunities for noninvasive, real-time monitoring of human sweat biomarkers from insensible sweat.

2. RESULT AND DISCUSSION

2.1. Design of the Insensible Sweat Sensor. The insensible sweat sensor features a superabsorbent PAAS/

https://doi.org/10.1021/acsnano.2c11267
ACS Nano 2023, 17, 5588−5599

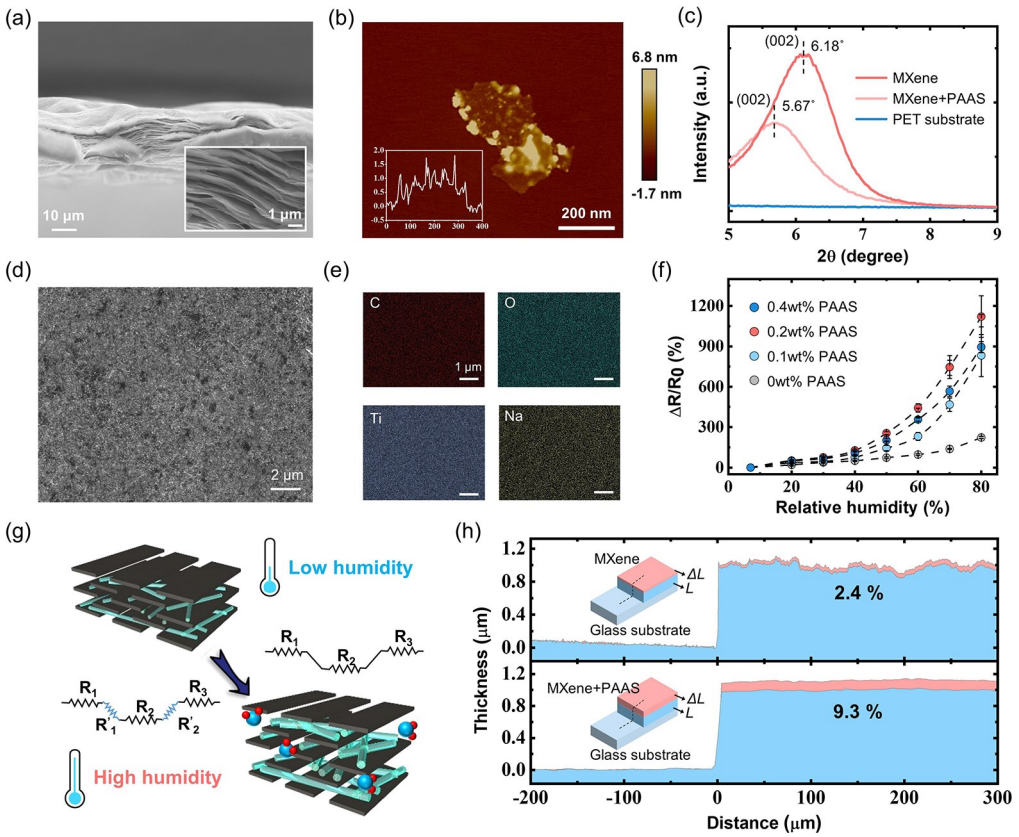

Figure 2. Structural and moisture-sensing characterizations of the MXene/PAAS composites. (a) SEM image of layered MXene nanosheets. (b) AFM image of the MXene nanosheet. (c) XRD patterns of the MXene (deep red), MXene/PAAS composite (light red), and PET substrate (blue). (d) SEM and (e) EDS image of the MXene/PAAS composite surface. (f) Normalized relative resistance changes of the MXene/PAAS composites with the PAAS mass fraction of 0, 0.1, 0.2, and 0.4 wt % as a function of the increasing RH from 7% to 80%. (g) Schematic showing the mechanism of the thickness changes in the MXene/PAAs composites film and (h) the measured thickness changes in the MXene and MXene/PAAs composites films as the RH increases from 45% to 80%.

MXene composite on a holey PET substrate sandwiched between two superhydrophobic textile layers. A child-friendly thin-film graphical overlay on the top encapsulates the sensor for minimized anxiety in pediatric patients,[39] and a double-sided medical adhesive on the bottom provides a robust interface to the skin for effective collection of insensible sweat (Figure 1b). Both the top graphical overlay and bottom adhesive layer are designed with a vent opening to allow the escape of sweat vapor and moisture from the skin to the environment (Figure S1). When designed to be superhydrophobic and waterproof, the porous breathable textile layers can prevent the insensible sweat sensor from being affected by inside sensible sweat or outside water. Connecting the insensible sweat sensor to a reusable flexible printed circuit board (FPCB) further provides the sensor with signal processing and wireless transmission (Figure 1c). The FPCB (length of 2.5 cm and width of 3 cm) with the block system-level diagram shown in Figure 1d and the circuit diagram shown in Figure S2 remains functional even upon severe deformations (Figure S3). The signals acquired through voltage dividers and the analog-to-digital converter (ADC) are wirelessly transmitted to the user graphic interface via Wi-Fi. The determined insensible sweat rate from various body parts at different ambient temperatures evaluates the health conditions, skin barrier functions, and the thermal comfort of the human body (especially for infants or others with aphasia) (Figure 1e).

2.2. Characterization of MXene/PAAS Composites for Moisture Sensing. The fabrication of the MXene/PAAS composite hydration sensors starts with the drop-coating of the aqueous solution of MXene/PAAS composite onto the commercially available PET substrate with copper electrodes connected on both ends (Figure S4). In brief, selectively etching Al in the MAX matrix with a mixed solution of hydrochloric acid and lithium fluoride results in MXene (or $Ti_3C_2T_x$) nanosheets with layered structures, as shown in the scanning electron microscope (SEM) image (Figure 2a). The thickness is determined to be ca. 1.5 nm from the atomic force microscope (AFM) image (Figure 2b). The disappeared 104 peaks (⍰39°) and the downshift of 002 peaks from 9.5° to 6.18° in the X-ray diffraction (XRD) also confirm the successful synthesis of the MXene with increased interplanar spacing due to the introduced functional groups and water (Figure S5, a).[40] The Tyndall effect of the resulting aqueous solution of the MXene nanosheets in water indicates a homogeneous dispersion (Figure S5, b). Next, the PAAS powders dissolved in the $Ti_3C_2T_x$ dispersion are sprayed on the PET surface to form the composite with the PAAS molecules tightly attached to the stacked $Ti_3C_2T_x$ sheet, as confirmed by the SEM and corresponding EDS mapping (Figure 2d,e). The resulting dispersion shows long-term stability without precipitation after a month (Figure S6). The further shifted 002 peaks of MXene−PAAS composites from 6.18° to 5.67° confirm the successful insertion of PAAS molecules between the MXene layers as described in ref 41. The numerous functional groups in the PAAS evenly distributed on the MXene nanosheets enhance the adsorption of water molecules,[42]

https://doi.org/10.1021/acsnano.2c11267
ACS Nano 2023, 17, 5588−5599

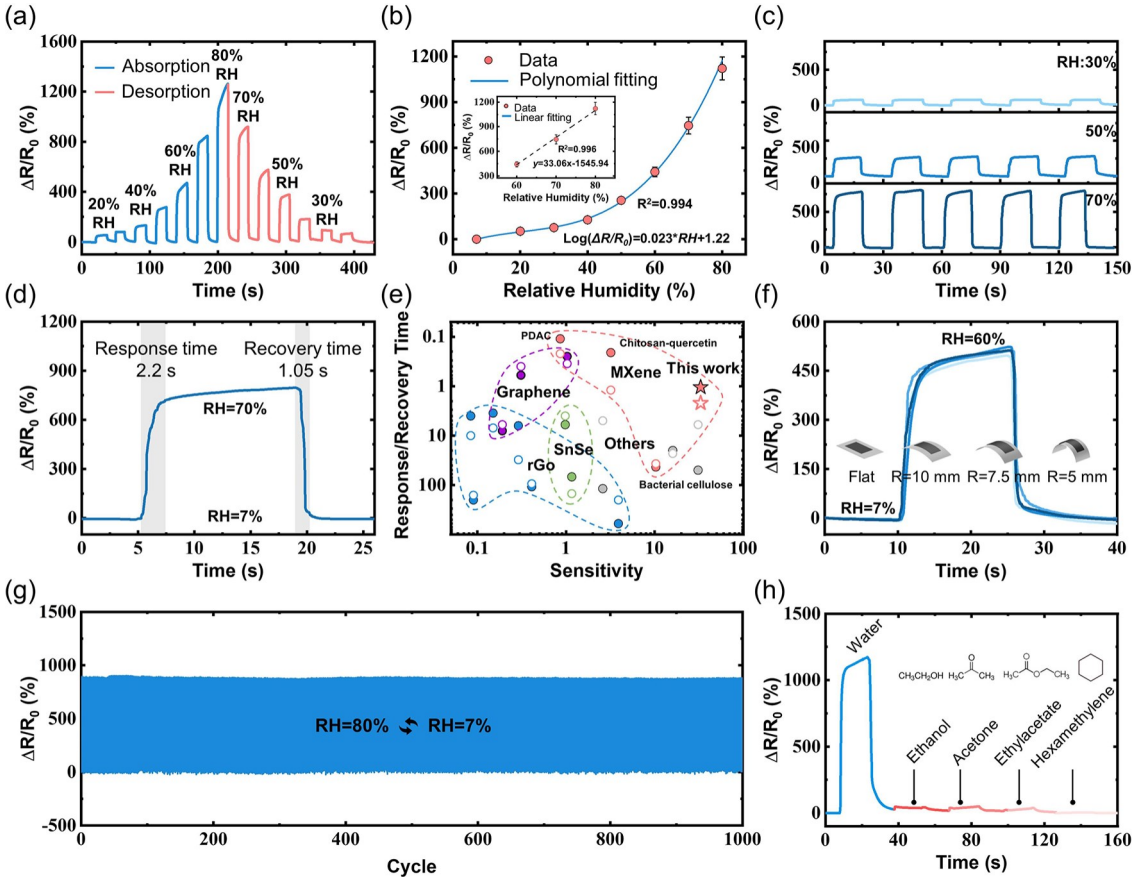

Figure 3. Performance evaluation of the humidity sensor. (a) Dynamic response and recovery curves of the sensor as the RH progressively increases from 7% to 80% and returns. (b) Calibration curve of the humidity sensor. (c) Stability testing of the humidity sensor at the RH of 30%, 50%, and 70%. (d) Response and recovery times of the humidity sensor as the RH switches between 7% and 70%. (e) Performance comparison in the response/recovery time and sensitivity between the humidity sensor from this study and others previously reported in the literature. (f) Response curves of the humidity sensor at different bending states under 60% RH. (g) Cyclic reliability test of the humidity sensor between the an RH of 7% and 80% over 1000 cycles. (h) Selectivity of the humidity sensor over various polar volatile organic compounds (7% RH).

resulting in significantly enhanced responses to changes in the relative humidity (RH) from 7% to 80% (Figure 2f). As the mass fraction of the PAAS increases in the composite (from 0 to 0.4 wt %), the normalized relative resistance change ($\Delta R/R_0$) of the humidity sensor first increases and then decreases, with a peak response at 0.2 wt %. The declined performance at higher mass fractions results from the larger interlayer spaces and fewer conductive pathways between MXene layers for excessive molecules. As a result, the composite with the optimum 0.2 wt % PAAS exhibits a much larger thickness change of 9.2% than that of 2.4% from the MXene sheets alone, for the increased RH from 45% to 80% (Figure 2g,h). Therefore, the composite with 0.2 wt % PAAS is selected in the following investigations unless specified otherwise.

2.3. Nonholey and Holey Designs of the Insensible Sweat Sensor. The current−voltage characteristics of the composite on the nonholey PET in varying RH values exhibit Ohm's behavior, and the slope decreases with the increasing RH due to increased resistance (Figure S7). The progressively increased and then decreased RH from 7% to 80% characterizes the adsorption and desorption process of water molecules in the composite (Figure 3a). The almost symmetric shape in the response curve and full recovery to its initial value demonstrate reversibility and little hysteresis of the humidity sensor (Figure S8). As the RH increases, the sensitivity (or the slope in the $\Delta R/R_0$ vs RH curve) is initially small but is followed by a rapid increase to achieve 33.06 in the RH range of 60% to 80% (Figure 3b). The exponential dependence of the sensor response $\Delta R/R_0$ on the RH further yields a linear fit: $\log(\Delta R/R_0) = 0.023 \times \mathrm{RH} + 1.22$, with a coeficient of determination of 0.994. The response of the composite at different RH values (30%, 50%, and 70%) exhibits high repeatability over five cycles (Figure 3c). The response and recovery of the composite are also rapid, with a response/recovery time of 2.2 s/1.05 s as the RH switches from 7% to 70% (Figure 3d). The composite with ultrahigh sensitivity and rapid response/recovery to accurately and rapidly detect humidity changes compares favorably to those reported in the previous literature (Figure 3e and Table S1).[36−38,43−58] Moreover, the use of the thin PET substrate with the composite allows it to bend over hundreds of cycles (Figure S9) with negligible response changes. As a result, the sensor in four different bending states (i.e., flat or with a radius of R = 10, 7.5, or 5 mm) can still accurately detect the humidity changes (Figure 3f). The long-term stability and durability of the sensor are also confirmed as the RH is cycled between 7% and 80% (Figure 3g). As the elevated temperature lowers the adsorption energy to decrease the amount of adsorbed water molecules, the sensor response is reduced as the temperature increases from 19 to 45 °C (Figure S10). However, the temperature variation at the skin surface is small and usually within 37−40 °C, so the change in

https://doi.org/10.1021/acsnano.2c11267
ACS Nano 2023, 17, 5588−5599

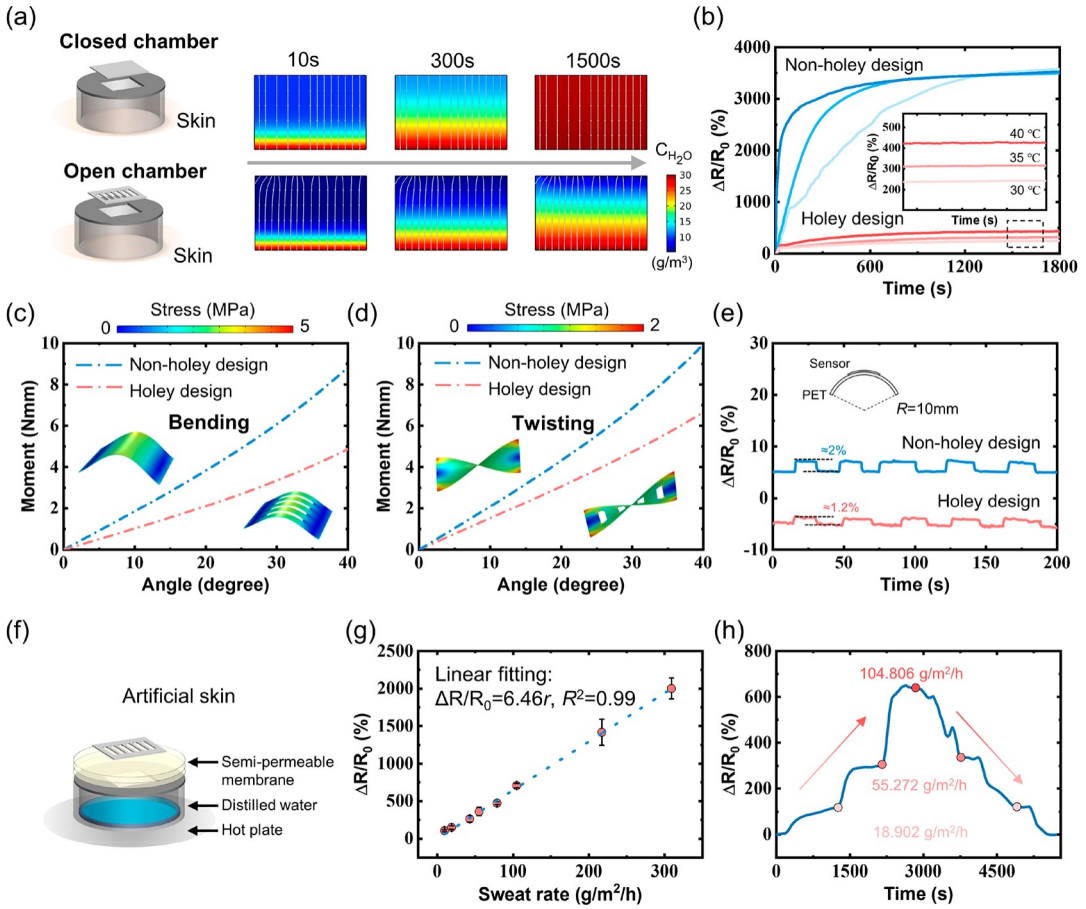

Figure 4. Performance characterizations of the nonholey and holey insensible sweat sensors. (a) Schematic showing the commonly used insensible sweat detection strategies (i.e., open and closed chamber) and the corresponding diffusion process of water molecules from the simulation. (b) Normalized relative resistance changes of holey and nonholey insensible sweat sensors at different temperature-induced water evaporation rates. Comparisons of (c) bending and (d) twisting stiffnesses between holey and nonholey device designs, with the deformed geometries and stress distributions in the PET substrate from the simulation shown in the insets. (e) Normalized relative resistance changes of holey and nonholey sensors during the repeated bending for a bending radius of 10 mm. (f) Schematic showing the artificial skin based on the wet-cup method. (g) Calibration curve of the holey insensible sweat sensor for the sweat rate from 9.64 to 309.01 g/m^2/h. (h) The time-dependent response from the sensor for stepwise increased and decreased sweat rates (18.902, 55.272, and 104.806 g/m^2/h).

sensing performance from the temperature is negligible compared to the changes caused by the RH. Furthermore, the excellent selectivity of the sensor is confirmed by its significantly higher response to water molecules (80% RH) over a wide range of other interfering polar volatile organic compounds, including ethanol, acetone, ethyl acetate, and hexamethylene (7% RH) (Figure 3h).

The use of nonholey PET toward a closed-chamber design is challenging for continuous long-term insensible sweat monitoring due to quick saturation.[7] In contrast, the holey PET substrate prepared by CO_2 laser cutting (Figure S11) allows moisture exchange with the environment to create a relatively steady concentration gradient of water molecules for long-term monitoring (Figure 4a). In the simulated sweat vapor experiment with evaporation rate controlled by the temperature (30, 35, and 40 °C), the nonholey insensible sweat sensor shows a large and rapid increase, but it quickly saturates and cannot distinguish the different water evaporation rates (Figure 4b). In contrast, the holey insensible sweat sensor exhibits a response that clearly depends on the evaporation rate. The holey design also reduces the effective bending stiffness by 60.15% (from 12.8 to 5.1 N mm/rad, Figure 4c) and twisting stiffness by 31.11% (from 13.5 to 9.3 N mm/rad, Figure 4d), improving the level of comfort and reducing mechanically induced skin irritation.[59] Compared with the nonholey one, the holey design shows reduced resistance change affected by mechanical deformation such as bending (e.g., 1.2% vs 2% for a bending radius of 10 mm) (Figure 4e). An artificial skin (beaker with water covered with a semipermeable membrane and placed on the hot plate) was used to simulate the skin sweating process based on the wet-cup method (Figure 4f). By changing the water temperature and thickness of the semipermeable membrane, the artificial skin can mimic the insensible sweat at a rate (r) from 9.64 to 309.01 g/m^2/h. The change in the normalized relative resistance of the holey insensible sweat sensor increases linearly with the increasing insensible sweat rate according to $\Delta R/R_0 = 6.46r$ (Figure 4g). The stable and reversible change in the sensor response with the initially increased and then decreased sweating rate also highlights the excellent dynamic sensing performance (Figure 4h), with small variations from the fan cooling process.

2.4. Superhydrophobic Fabric Encapsulation for Waterproof and Breathable Performance. To avoid performance degradation in hydrated environments such as inside sensible sweat or outside water, the insensible sweat sensor is encapsulated by the superhydrophobic fabric (Figure

https://doi.org/10.1021/acsnano.2c11267
ACS Nano 2023, 17, 5588−5599

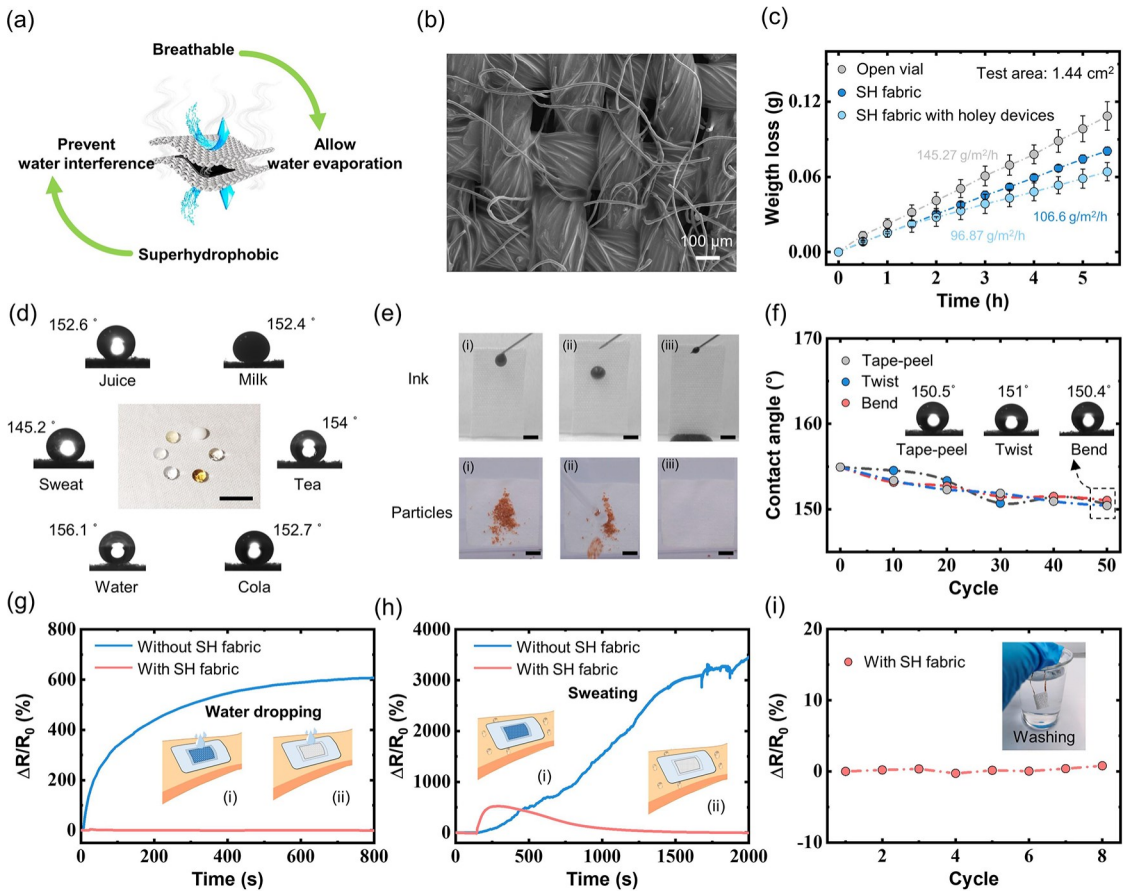

Figure 5. Waterproof and breathable insensible sweat sensors. (a) Schematic showing the sensing composite sandwiched between two superhydrophobic fabric layers. (b) SEM image of the superhydrophobic fabric. (c) Comparison of the evaporation rate between the open vial and holey insensible sweat sensor encapsulated with superhydrophobic fabric. (d) Liquids with different surface tensions (i.e., water, sweat, tea, cola, milk, and juice) on the superhydrophobic fabric, with the contact angle (CA) labeled (scale bar: 2 cm). (e) Cleaning of solid particles on the superhydrophobic fabric placed at an inclined angle with water droplets (scale bar: 1 cm). (f) The change in the CA of the water droplet on the superhydrophobic fabric as a function of tape-peeling, bending, and twisting cycles. Resistance responses of the hydration sensor with or without superhydrophobic fabric encapsulation during (g) water dropping and (h) human sweating. (i) Effect of washing cycles on the sensor response.

5a). The dip-coated silica (SiO_2) nanoparticles on the surface of the fabric provide micro/nanostructures with low surface energy, and further modification with poly(dimethylsiloxane) (PDMS) over SiO_2 increases the stability (Figure S12). The SiO_2 and PDMS coatings do not change the porous structure of the fabric (Figure 5b and Figure S13), and the superhydrophobic fabric still exhibits excellent breathability of 106.6 g/m^2/h (80% of 145.27 g/m^2/h from the completely open structure) (Figure 5c). After the integration of the superhydrophobic fabric with the holey sensor, the permeability of 96.87 g/m^2/h is still much higher than the maximum insensible sweat rate of 90 g/m^2/h.[7,60] A large contact angle (CA) is observed for various liquids (e.g., water, cola, juice, milk, tea, coffee, and sweat) on the superhydrophobic fabric, with a slightly smaller value for sweat due to the skin lipids in it (Figure 5d). The blue-dyed water droplets easily roll off the superhydrophobic fabric, so the solid particles can be eficiently removed by water for self-cleaning (Figure 5e). Because of the increased stability of the micro/nanostructures and robust hydrophobicity under mechanical deformation from the PDMS coating,[61,62] the fabric maintains a stable CA of >150° during repeated tape-peeling, squeezing, and twisting for 50 times (Figure 5f). The sensible sweat or water droplets not only easily wet the hydrophilic fabric but also penetrate into the functional layer to rapidly and irreversibly increase the resistance of the sensor (Figure 5g,h, blue). In contrast, the sensor with the superhydrophobic fabric encapsulation exhibits only a negligibly small relative resistance change after washing with water droplets from the outside (Figure 5g, red). Furthermore, the drastically reduced penetration of sensible sweat only leads to a small but reversible increase in the resistance response, which easily allows the sweat to completely evaporate for avoiding irreversible damage (Figure 5h, red). The superhydrophobic sensor is also not affected by washing cycles (Figure 5i), demonstrating robust performance in various hydrated environments.

2.5. Evaluation of Body Thermoregulation and Skin Barrier Functions. Connecting the breathable, superhydrophobic sweat sensor with a flexible wireless communication and powering module yields an integrated device with a small footprint to detect the insensible sweat from various human body parts (e.g., arm, forehead, and palms) (Figure 6a). Although differences exist among the three tested human subjects (Figure 6b), the insensible sweat rate from the arm (6.62, 8.84, 15.32 g/m^2/h) is much smaller than those from the forehead (38.36, 33.98, 29.81 g/m^2/h) or palms (67.71, 72.16,

https://doi.org/10.1021/acsnano.2c11267
ACS Nano 2023, 17, 5588−5599

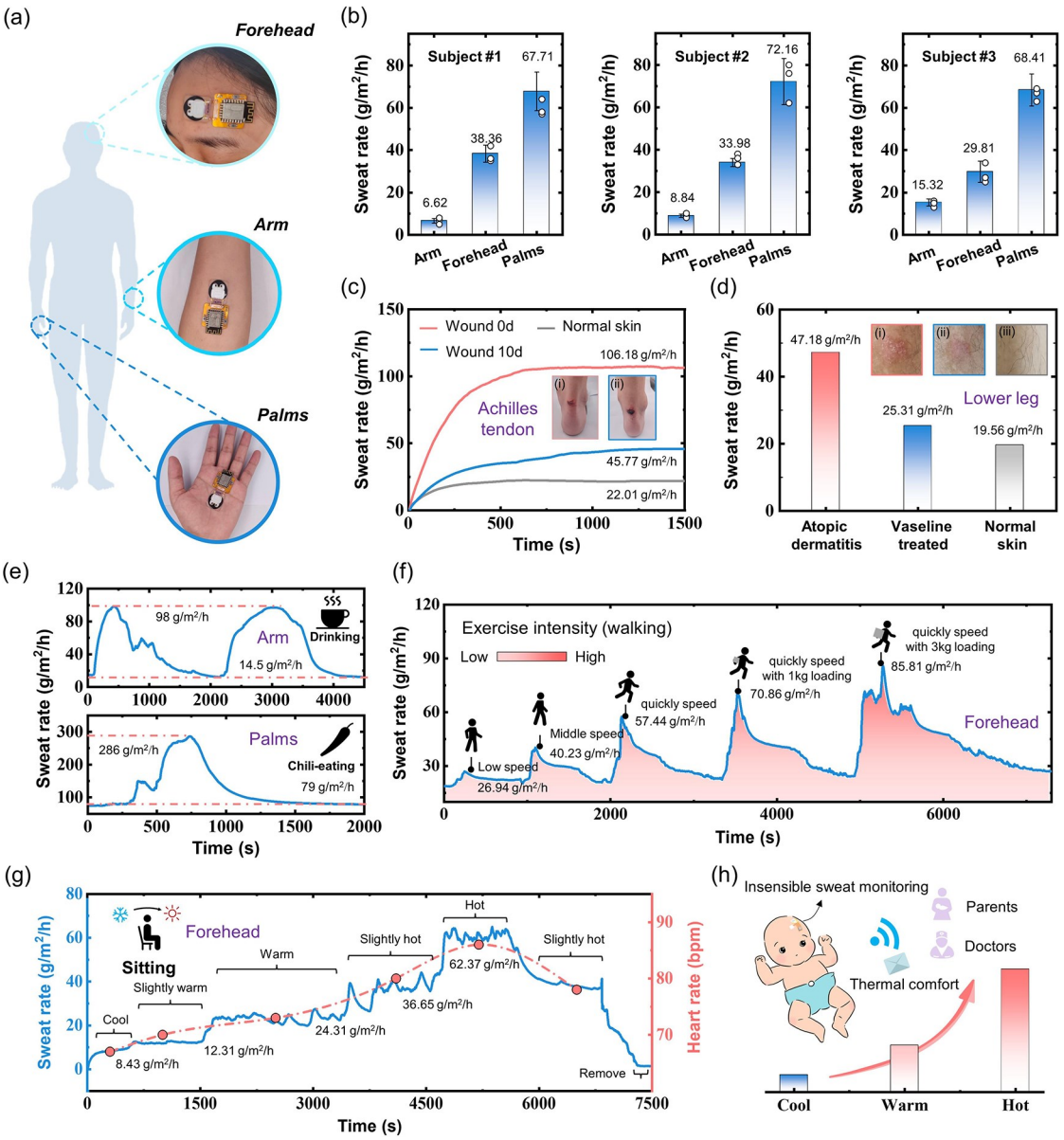

Figure 6. Integrated sweat sensing device system for real-time monitoring of insensible sweat. (a) Photographs showing the placement of the integrated device on different body parts for insensible sweat monitoring. (b) Comparison of the insensible sweat rate at different human body parts (arm, forehead, and palms) from three individuals, validated by a portable commercial moisture meter (hollow points). (c) Comparison of the insensible sweat rate at different Achilles tendon wound healing states (day 0, day 10, and normal skin). (d) Use of the insensible sweat rate from the lower leg to evaluate the effect of moisturizer on a participant diagnosed with AD. (e) Changes in the insensible sweat rates from the arm and palm after drinking hot water or eating peppers. (f) Continuous monitoring of insensible sweat rate from the forehead with different walking intensities. (g) Continuous monitoring of insensible sweat rate from the forehead and heart rate with different thermal states caused by variations in the ambient temperature. (h) Schematic showing the potential of the sensor for evaluating the thermal comfort of babies or patients with aphasia.

68.41 g/m^2/h). The results validated by the portable commercial moisture meter (gpskin Barrier, GPower Inc., Korea) are consistent with the previous reports.[63−65] Due to excellent breathability, the integrated device on the arm, forehead, and palm does not induce localized profuse sweating at 0, 30, and 60 min, as evidenced by the negligibly small difference in the insensible sweat changes between the places with and without the device (Figure S14). As skin acts as a protective barrier to effectively reduce water evaporation, the detection of the insensible sweat rate can be used to evaluate the integrity of skin barrier functions. For instance, mounting the integrated device on a wound in the Achilles tendon monitors the recovery of skin barrier functions (Figure 6c). Although the MXene and SiO_2 nanomaterials has been widely used for rapid hemostasis in wound healing,[66,67] there is still a lack of systematic analysis and evaluation of the long-term biosafety. In this study, SiO_2 and MXene fully encapsulated by the biocompatible PDMS layer are not directly applied on the skin surface (but through a double-sided medical tape), so the toxicity of the materials is of less concern. As the wound heals, the insensible sweat rate gradually decreases from 106.18 g/m^2/h to 45.77 g/m^2/h on day 10 and 22.01 g/m^2/h after complete wound healing on day 60. The integrated device mounted onto the calf can identify skin diseases such as atopic dermatitis (AD)

https://doi.org/10.1021/acsnano.2c11267
ACS Nano 2023, 17, 5588−5599

with a higher insensible sweat rate (47.18 g/m^2/h) over the nonlesion sites (19.56 g/m^2/h) (Figure 6d), which is consistent with the clinical symptoms of the lesions.[68] The insensible sweat sensor can also evaluate the treatment response of a moisturizer that brings the insensible sweat rate down to 25.31 g/m^2/h with Vaseline.

The changes in the insensible sweat rate can also reflect the body's thermoregulation. When drinking water at a temperature of 55 °C, the thermoreceptors in the oral cavity sense the increased temperature to start thermoregulatory functions.[69] As a result, the insensible sweat rate increases from 14.5 to 98 g/m^2/h and soon recovers to its initial level (Figure 6e, top). As the capsaicin in the chili pepper can activate the thermoreceptors in the oral cavity to result in significant thermoregulatory function,[70] eating spicy chili induces gustatory sweating to increase the sweat rate from 79 (insensible) to 286 g/m^2/h (sensible), followed by a return to the baseline after 20 min (Figure 6e, bottom). The body's thermoregulation also regulates metabolic heat generated from brain activities,[71] implying the potential to monitor psychological activities with an insensible sweat rate. The simulated brain activities from watching and discussing funny videos are captured by the increased palm sweat rate from 71.11 (at rest) to 90.75 (during watching) and then to 71.23 g/m^2/h (at rest) (Figure S15 and Movie S1). Different from intense exercise to cause a high sensible sweat rate, mild/low exercise (e.g., walking or jogging) results in a low insensible sweat rate, which is dificult to measure with previously reported sweat sensors. However, our integrated device can continuously track the insensible sweat rate from human subjects engaging in a range of walking intensities, including slow walking, medium-fast walking, fast walking, and fast walking with a load of 2 and 5 kg (Figure 6f). The insensible sweat rate progressively increases from 26.94 to 85.81 g/m^2/h as the walking intensity increases from slow walking to fast walking with a load of 5 kg. The continuously measured insensible sweat rate also allows the accurate calculation of the sweat loss over time (the area under the curve) to help evaluate the current hydration status.

The thermal comfort of the occupants in built environments can also be conveniently evaluated by the insensible sweat sensor. By switching the thermal state from cold (16 °C) to hot (32 °C) with steps of 4 °C in the environment temperature, the integrated device placed on the forehead shows a gradually increased insensible sweat rate: 8.43, 12.31, 24.31, 36.65, and 62.37 g/m^2/h (Figure 6g). The insensible sweat rate also returns to the initial value after switching the thermal state back to the cold, demonstrating the reversibility of the device. The measured insensible sweat rate from the palm also shows a gradual increase: 22.65, 31.48, 45.69, 69.15, and 96.51 g/m^2/h (Figure S16), showing a similar trend to that from the forehead (Figure S17) to reveal the body thermoregulation. The direct measurement of thermal status from the insensible sweat rate demonstrates the high potential of the integrated devices to evaluate the thermal comfort of babies or patients with aphasia (Figure 6h). The integrated sweat sensing system may also be combined with the other electrochemical sensors to provide potential application opportunities in the noninvasive detection of biomarkers from insensible sweat.

3. CONCLUSION

In summary, this work reports the skin-interfaced sweat sensing device to continuously and wirelessly measure insensible sweat loss for evaluating the body thermoregulation and skin barrier functions in all weather conditions (Table 1). The superabsorbent PAAS/MXene composite exhibits significantly enhanced sensitivity and rapid response, whereas the waterproof and breathable superhydrophobic textile encapsulation layers effectively prevent the sensor performance from being affected by external hydrated environments such as sensible sweat or washing. With a flexible wireless transmission and powering module, the integrated device can be conveniently attached to various body parts of freely moving human subjects to continuously detect insensible sweat. The proof-of-concept demonstrations include the evaluation of skin barrier functions, psychological activities via the body's thermoregulation, and thermal comfort. The results from this work could also be combined with other electrochemical sensors to result in the next-generation sweat monitoring device for detecting biomarkers from insensible sweat in the future.

4. EXPERIMENTAL SECTION

4.1. Synthesis of $Ti_3C_2T_x$ MXene Nanosheets and MXene/PAAS Dispersions. $Ti_3C_2T_x$ (MXene) nanosheets were synthesized by selectively etching the Al phase from the MAX (Ti_3AlC_2) phase (11 Technology Co., Ltd.) with LiF/HCl as previously reported.[40] In a typical procedure, 3.2 g of LiF (Aladdin) was slowly dissolved in 40 mL of 9 M HCl (Aladdin) in a Teflon container under magnetic stirring for ca. 1 h to ensure the complete dissolution of LiF. Next, 2 g of Ti_3AlC_2 powder was slowly added to the LiF/HCl etching solution (within 5 min), and the mixture was allowed to react at 35 °C under magnetic stirring for 24 h to form a stable suspension. The resulting $Ti_3C_2T_x$ suspension was repeatedly washed with deionized water and centrifuged at 3500 rpm for 5 min until the supernatant exhibited a dark green color with a pH greater than 5. The swollen black $Ti_3C_2T_x$ slurry was redissolved by adding 40 mL of deionized water to the entire sediment. After centrifugation at 3500 rpm for 2 min, the dark concentrated supernatant of $Ti_3C_2T_x$ nanosheets was collected. Further delamination of $Ti_3C_2T_x$ was performed by sonication followed by centrifugation at 3500 rpm for 1 h, resulting in a homogeneous supernatant containing delaminated $Ti_3C_2T_x$ nanosheets. The concentration of the resulting colloidal MXene solution was determined by filtering a known volume of the solution through a polypropylene filter (0.22 μm, Celgard 3501 coated PP) and measuring the weight of the resulting free-standing film after vacuum drying. Further dilution of the resulting colloidal MXene solution gave an MXene solution of 2 mg mL^{-1}. Finally, the MXene/PAAS dispersions with different mass fractions of PAAS (Aladdin, average $M_w = 3 \times 10^6$ to 7 $\times$ 10^6) were obtained by mixing the diluted MXene solution (10 mL, 2 mg mL^{-1}) with PAAS powders (0 mg, 10 mg, 20 mg, 40 mg) under magnetic stirring for 1 h (marked as 0, 0.1, 0.2, and 0.4 wt %, respectively).

4.2. Preparation of the MXene/PAAS Humidity Sensor. The MXene/PAAS humidity sensor was designed with a holey PET substrate, silver electrodes, and an MXene/PAAS composite film. PET substrates were patterned with designed holes by laser cutting (commercial ultraviolet laser with a power of 60 W, beam diameter of 10 μm, and cutting speed of 700 mm/s). Silver electrodes were fabricated on the holey PET substrate by screen printing and baking in an oven at 80 °C for 1 h. Next, the holey PET substrate was treated with air plasma (high power level for 3 min) to give a hydrophilic surface. The MXene/PAAS solution was then drop-cast on the PET substrate to form a moisture-sensing layer, with the thickness controlled by the drop volume. Finally, the copper wires were attached on two ends of the electrodes using silver paint (CD-03, Kaixiang Electronic Co., Ltd.) for connection to the data acquisition device.

4.3. Preparation of the Superhydrophobic Fabric. The superhydrophobic fabric was fabricated by a two-step dip-coating process in a hydrophobic SiO_2 nanoparticle solution and a PDMS solution. Then 2.4 g of hydrophobic SiO_2 nanoparticles (R202, Evonik Industries Co. Ltd., Germany) were ultrasonically dispersed in 100 mL of ethanol for 1 h for homogeneous mixing to yield a hydrophobic SiO_2

https://doi.org/10.1021/acsnano.2c11267
ACS Nano 2023, 17, 5588−5599

Table 1. Performance Comparison between Our Integrated Sweat Sensing Device System and Previous Reports[6,12,15,21,27,71,72]

Strategy	Text description	Anti-water-interference	Continuous monitoring	Insensible sweat measure	Maximum sensitivity	Wireless monitoring	Functions	ref
Microfluidic devices	Incorporation of a hydrophilic filler in the sweat collection well to reduce the volume of sweat that must be accumulated before it is pushed into the channel for measurement	No	No	No (sweat gland secreting)	0.6 g/m^2/h	No	Thermoregulation analysis	15
Humidity sensor (commercial)	Incorporation of a humidity sensor in the truncated hollow cone and a actuator was needed for natural ventilation	No	No	Yes	0.0111 (%/s)/(g/m^2/h)	No	Insensible sweat loss detecting	21
Humidity sensor (commercial)	Incorporation of a humidity sensor in the closed chamber with thermo-pneumatic actuator for natural ventilation	No	No	Yes	0.039 (pF/s)/(g/m^2/h)	No	Thermal comfort monitoring	6
Humidity sensor (homemade)	Breathable PVA nanomesh with Au coats	No	Yes	No	25% (98% RH)	No	Skin humidity	27
Humidity sensor (homemade)	Humidity sensor composed of nanomesh Au electrodes and nanomesh humidity-sensitive materials	No	Yes	No	1 390 000% (97% RH)	No	Skin humidity	72
Humidity sensor (homemade)	Polydopamine-modified acid-treated carbon nanotubes	No	Yes	No	350% (90% RH)	No	Skin humidity	71
Humidity sensor (homemade)	$ZnIn_2S_4$ nanosheet-based humidity sensor	Yes	Yes	No	70% (90% RH)	Yes	Skin humidity	12
Humidity sensor (homemade)	MXene/PAAS based holey-designed humidity sensor with superhydrophobic and breathable fabric encapsulation	Yes	Yes	Yes	6.46 ($\Delta R/R_0$)/(g/m^2/h)	Yes	Thermoregulation analysis and skin barrier function evaluation	This work

nanoparticle solution. To prepare the PDMS solution, 0.1 g of PDMS prepolymer (Sylgard 184A) and 0.01 g of curing agent (Sylgard 184B) were added to 100 mL of *n*-hexane followed by ultrasonication for 15 min. In the first dip-coating process, the cleaned fabric (2 cm × 2 cm) was dipped into the hydrophobic SiO_2 nanoparticle solution for 10 min, followed by drying at room temperature. Next, the dried fabric was immersed into the PDMS solution for 120 s, and curing at 80 °C for 5 h yielded the superhydrophobic fabric.

4.4. Integration of Insensible Sweat Sensors. The MXene/PAAS humidity sensor was first encapsulated between two pieces of superhydrophobic fabrics, and superhydrophobic treated wires were used for the connection. The cartoon image in the child-friendly thin-film graphical overlay was fabricated by a laser printer (HP color laser 150nw) on a commercial PET-based tape. The double-sided medical adhesive (1524, 3M) and graphical overlay were provided with a vent opening by laser cutting. Next, these components were stacked in sequence (from bottom to top: adhesive layer, superhydrophobic fabric encapsulated humidity sensor, and child-friendly thin-film graphical overlay) and pressed to obtain the integrated insensible sweat sensor.

4.5. Finite Element Analysis of the Sweat Diffusion Process. Finite element analysis of the sweat diffusion in a closed and open chamber was performed using the transport of a diluted species module in commercially available software (COMSOL Multiphysics 5.6, COMSOL, Sweden). A 2D model of the chamber with a width of 15 mm and thickness of 10 mm was created with holes (normalized length $l/a = 1/2$) on the top to simulate the holey design. The sweat diffusion process follows Fick's second law: $\partial c/\partial t = D\nabla^2 c$, where c is the concentration and D is the diffusion coeficient (1×10^{-4} m^2/s in this case). For the closed chamber, the concentration of sweat was assumed to be a constant of 3×10^{-8} mol/m^3 at the bottom with zero flux at the other boundaries. For the open chamber, the concentration was set as 5.9×10^{-9} mol/m^3 on the top hole, with the others to be the same as the closed-chamber design.

4.6. Mechanical Analysis of the Holey and Nonholey PET Substrates. The mechanical properties of holey and nonholey PET substrates subjected to bending and twisting were simulated in COMSOL. The periodic holes with a spacing of 2 mm and a width of 1 mm were created in the holey PET substrate with a size of 14 mm × 14 mm and a thickness of 0.05 mm. After setting a pair of edges free, the same torsion (or bending) angle from 0 to 40° was applied to the other pair of edges to compare the moment between the holey and nonholey PET substrates. The Young's modulus (E) of the PET substrate was $E_{PET} = 4$ GPa.

4.7. Characterizations. The sample morphology was analyzed by a field emission scanning electron microscope (SU5000, Hitachi, Japan) at an accelerating voltage of 25 kV. Energy-dispersive X-ray spectroscopy (EDX) and mapping were also acquired with the same equipment. XRD curves were recorded on an X'Pert PRO XRD using Cu Kα radiation and a scanning speed of 5°/min. The contact angles of the samples were measured using a model 250 (p/n 250-F1) optical contact-angle goniometer (Rame-hart, USA) at ambient temperature. The average CA was obtained from measurements at more than five different positions on the same sample. The electrical characteristics of the strain sensor were measured using a digital source meter (2400, Keithley Instruments, Inc., Cleveland, OH, USA). The thickness changes of the $Ti_3C_2T_x$ film and $Ti_3C_2T_x$/PAAS composite film in different humidity environments were characterized by Profilm 3D (America, Filmetrics). Humidity-sensing characteristics were tested in a closed bottle with varying chamber humidity levels at a constant temperature of 25 °C. Different humidity levels were obtained by controlling the sulfuric acid concentration, with the actual humidity value measured by a commercial humidity sensor (Testo, 605-H1).

4.8. Human Experiment. The insensible sweat rate from various human body parts was measured in a controlled environment with an RH level of 30−40% and temperature of 28 °C unless otherwise specified. The area of measurement was ca. 3.14 cm^2 (the size of the vent opening on the bottom adhesive layer). The measurement location was washed with soap and dried, followed by sitting still for 30 min before testing. Readings taken in triplicate from the portable

https://doi.org/10.1021/acsnano.2c11267
ACS Nano 2023, 17, 5588−5599

commercial moisture meter (gpskin Barrier, GPower Inc., Korea) on the same site served as a metric for comparison and validation.

ASSOCIATED CONTENT

*** Supporting Information**

The Supporting Information is available free of charge at https://pubs.acs.org/doi/10.1021/acsnano.2c11267.

Photographs of the insensible sweat sensing device; circuit diagram of the FPCB for signal processing and wireless communication; image of the FPCB upon deformation; schematic showing the fabrication process of the MXene/PAAS humidity sensor with or without the patterned structure; characterization of MXene nanosheets; photographs of the MXene/PAAS solution before and after storing for 30 days; *I*−*V* curves of the humidity sensor at different RH levels; hysteresis of the humidity sensor in the RH range from 7% to 80%; stability of the humidity sensor to 40% RH under multiple bending cycles; effect of temperature on the response of the humidity sensor; design of the holey PET substrate; contact angle of water on pristine fabric, PDMS-modified fabric, and SiO_2- and PDMS-modified fabric; SEM image of the fabric before surface modification; comparison in the TEWL between the places with and without the device at 0, 30, and 60 min on different body locations; continuous monitoring of the insensible sweat rate from different brain activities; continuous monitoring of the insensible sweat rate from the palm at different thermal states caused by variations in the ambient temperature; comparison of the insensible sweat rate between the palm and forehead at different thermal states caused by variations in the ambient temperature; performance comparison between our sensor and other humidity sensors (PDF)

Movie S1: Continuous monitoring of the insensible sweat rate from different brain activities (MP4)

AUTHOR INFORMATION

Corresponding Authors

Huanyu Cheng − *Department of Engineering Science and Mechanics, The Pennsylvania State University, University Park, Pennsylvania 16802, United States;* orcid.org/0000-0001-6075-4208; Email: Huanyu.Cheng@psu.edu

Xiufeng Wang − *School of Materials Science and Engineering, Xiangtan University, Xiangtan, Hunan 411105, China;* orcid.org/0000-0002-9557-049X; Email: onexf@xtu.edu.cn

Authors

Yangchengyi Liu − *School of Materials Science and Engineering, Xiangtan University, Xiangtan, Hunan 411105, China*

Xiaofeng Li − *School of Materials Science and Engineering, Xiangtan University, Xiangtan, Hunan 411105, China*

Hanlin Yang − *School of Materials Science and Engineering, Xiangtan University, Xiangtan, Hunan 411105, China*

Ping Zhang − *School of Materials Science and Engineering, Xiangtan University, Xiangtan, Hunan 411105, China*

Peihe Wang − *School of Materials Science and Engineering, Xiangtan University, Xiangtan, Hunan 411105, China*

Yi Sun − *School of Materials Science and Engineering, Xiangtan University, Xiangtan, Hunan 411105, China*

Fengzhen Yang − *School of Materials Science and Engineering, Xiangtan University, Xiangtan, Hunan 411105, China*

Weiyi Liu − *School of Materials Science and Engineering, Xiangtan University, Xiangtan, Hunan 411105, China*

Yujing Li − *School of Materials Science and Engineering, Xiangtan University, Xiangtan, Hunan 411105, China*

Yao Tian − *School of Chemistry, Xiangtan University, Xiangtan, Hunan 411105, China*

Shun Qian − *School of Chemistry, Xiangtan University, Xiangtan, Hunan 411105, China*

Shangda Chen − *School of Materials Science and Engineering, Xiangtan University, Xiangtan, Hunan 411105, China*

Complete contact information is available at: https://pubs.acs.org/10.1021/acsnano.2c11267

Author Contributions

Y.L., X.L., H.Y., and P.Z. contributed equally to this work. X.F.W. and H.Y.C. directed the research, X.F.W., H.Y.C., and Y.C.Y.L. conceived the idea and designed the research. Y.C.Y.L. carried out and participated in all the experiments. Y.C.Y.L., X.F.L., and H.L.Y. conducted materials characterization, holey-design sensor sensing, and superhydrophobic performance test. P.Z. conducted the nonholey design sensor sensing performance and partial materials characterization. Y.C.Y.L. and P.H.W. conducted synthesis of MXene nanosheets. Y.S. performed the FEA simulations and analyses. F.Z.Y., Y.T., and S.Q. designed the wireless sensor module. X.F.L., H.L.Y., W.Y.L., and Y.J.L. participated in the experiment on insensible sweat monitoring. S.D.C. provided the portable commercial moisture meter. Y.C.Y.L., X.F.L., H.L.Y., W.Y.L., and S.D.C. participated in the experiment on insensible sweat monitoring. All the authors discussed the results. Y.C.Y.L., X.F.W., and H.Y.C. wrote the manuscript with help from all authors.

Notes

The authors declare no competing financial interest.

ACKNOWLEDGMENTS

This research was supported by the National Natural Science Foundation of China (12172319 and 11872326), Natural Science Foundation of Hunan Province (2021JJ30648 and 2021JJ30641), Scientific Research Fund (22A0130) of Hunan Provincial Education Department, and Furong Scholars Programme of Hunan Province. H.C. also acknowledges the support from the National Institutes of Health (Award Nos. R21EB030140, U01DA056242, and R61HL154215), the National Science Foundation (NSF) (Grant Nos. ECCS-2222654 and 1933072), and Penn State University.

REFERENCES

(1) Vriens, J.; Nilius, B.; Voets, T. Peripheral thermosensation in mammals. *Nat. Rev. Neurosci* 2014, *15*, 573−89.

(2) Fang, Y.; Chen, G.; Bick, M.; Chen, J. Smart textiles for personalized thermoregulation. *Chem. Soc. Rev.* 2021, *50*, 9357−9374.

(3) Hu, R.; Liu, Y.; Shin, S.; Huang, S.; Ren, X.; Shu, W.; Cheng, J.; Tao, G.; Xu, W.; Chen, R.; Luo, X. Emerging Materials and Strategies for Personal Thermal Management. *Adv. Energy Mater.* 2020, *10*, 1903921.

(4) Cramer, M. N.; Gagnon, D.; Laitano, O.; Crandall, C. G. Human temperature regulation under heat stress in health, disease, and injury. *Physiol. Rev.* 2022, *102*, 1907.

(5) Periard, J. D.; Eijsvogels, T. M. H.; Daanen, H. A. M. Exercise under heat stress: thermoregulation, hydration, performance implications, and mitigation strategies. *Physiol. Rev.* 2021, *101*, 1873−1979.

(6) Sim, J. K.; Yoon, S.; Cho, Y. H. Wearable Sweat Rate Sensors for Human Thermal Comfort Monitoring. *Sci. Rep.* 2018, *8*, 1181.

(7) Zhong, B.; Jiang, K.; Wang, L.; Shen, G. Wearable Sweat Loss Measuring Devices: From the Role of Sweat Loss to Advanced Mechanisms and Designs. *Adv. Sci.* 2022, *9*, 2103257.
(8) Nie, S.; Zhang, C.; Song, J. Thermal management of epidermal electronic devices/skin system considering insensible sweating. *Sci. Rep.* 2018, *8*, 14121.
(9) Koh, A.; Kang, D.; Xue, Y.; Lee, S.; Pielak, R. M.; Kim, J.; Hwang, T.; Min, S.; Banks, A.; Bastien, P.; Manco, M. C.; Wang, L.; Ammann, K. R.; Jang, K.-I.; Won, P.; Han, S.; Ghaffari, R.; Paik, U.; Slepian, M. J.; Balooch, G.; Huang, Y.; Rogers, J. A. A soft, wearable microfluidic device for the capture, storage, and colorimetric sensing of sweat. *Sci. Transl. Med.* 2016, *8*, 366ra165−366ra165.
(10) Zhang, Y.; Chen, Y.; Huang, J.; Liu, Y.; Peng, J.; Chen, S.; Song, K.; Ouyang, X.; Cheng, H.; Wang, X. Skin-interfaced microfluidic devices with one-opening chambers and hydrophobic valves for sweat collection and analysis. *Lab Chip* 2020, *20*, 2635−2645.
(11) Nyein, H. Y. Y.; Bariya, M.; Kivimaki, L.; Uusitalo, S.; Liaw, T. S.; Jansson, E.; Ahn, C. H.; Hangasky, J. A.; Zhao, J.; Lin, Y.; Happonen, T.; Chao, M.; Liedert, C.; Zhao, Y.; Tai, L. C.; Hiltunen, J.; Javey, A. Regional and correlative sweat analysis using high-throughput microfluidic sensing patches toward decoding sweat. *Sci. Adv.* 2019, *5*, eaaw9906.
(12) Lu, Y.; Fujita, Y.; Honda, S.; Yang, S. H.; Xuan, Y.; Xu, K.; Arie, T.; Akita, S.; Takei, K. Wireless and Flexible Skin Moisture and Temperature Sensor Sheets toward the Study of Thermoregulator Center. *Adv. Healthcare Mater.* 2021, *10*, No. e2100103.
(13) Baker, L. B.; Seib, M. S.; Barnes, K. A.; Brown, S. D.; King, M. A.; De Chavez, P. J. D.; Qu, S.; Archer, J.; Wolfe, A. S.; Stofan, J. R.; Carter, J. M.; Wright, D. E.; Wallace, J.; Yang, D. S.; Liu, S.; Anderson, J.; Fort, T.; Li, W.; Wright, J. A.; Lee, S. P.; Model, J. B.; Rogers, J. A.; Aranyosi, A. J.; Ghaffari, R. Skin-Interfaced Microfluidic System with Machine Learning-Enabled Image Processing of Sweat Biomarkers in Remote Settings. *Adv. Mater. Technol.* 2022, *7*, 2200249.
(14) Baker, L. B. Physiology of sweat gland function: The roles of sweating and sweat composition in human health. *Temperature* 2019, *6*, 211−259.
(15) Nyein, H. Y. Y.; Bariya, M.; Tran, B.; Ahn, C. H.; Brown, B. J.; Ji, W.; Davis, N.; Javey, A. A wearable patch for continuous analysis of thermoregulatory sweat at rest. *Nat. Commun.* 2021, *12*, 1823.
(16) Farahmand, S.; Tien, L.; Hui, X.; Maibach, H. I. Measuring transepidermal water loss: a comparative in vivo study of condenser-chamber, unventilated-chamber and open-chamber systems. *Skin Res. Technol.* 2009, *15*, 392−8.
(17) Matsukawa, R.; Miyamoto, A.; Yokota, T.; Someya, T. Skin Impedance Measurements with Nanomesh Electrodes for Monitoring Skin Hydration. *Adv. Healthcare Mater.* 2020, *9*, No. e2001322.
(18) Jansen van Rensburg, S.; Franken, A.; Du Plessis, J. L. Measurement of transepidermal water loss, stratum corneum hydration and skin surface pH in occupational settings: A review. *Skin Res. Technol.* 2019, *25*, 595−605.
(19) Chen, R.; Zhu, Z.; Ji, S.; Geng, Z.; Hou, Q.; Sun, X.; Fu, X. Sweat gland regeneration: Current strategies and future opportunities. *Biomaterials* 2020, *255*, 120201.
(20) Harker, M. Psychological sweating: a systematic review focused on aetiology and cutaneous response. *Skin Pharmacol. Physiol.* 2013, *26*, 92−100.
(21) Sim, J. K.; Ahn, B.; Doh, I. Truncated Hollow Cone Probe for Assessing Transepidermal Water Loss and Skin Hardness. *ACS Sens.* 2018, *3*, 2246−2253.
(22) Sim, D. J. K.; Kim, S. M.; Kim, S. S.; Doh, I. Portable Skin Analyzers with Simultaneous Measurements of Transepidermal Water Loss, Skin Conductance and Skin Hardness. *Sensors* 2019, *19*, 3857.
(23) Sim, J. K.; Cho, Y.-H. Portable sweat rate sensors integrated with air ventilation actuators. *Sens. Actuators B* 2016, *234*, 176−183.
(24) Ji, S.; Chen, X. Enhancing the interfacial binding strength between modular stretchable electronic components. *Natl. Sci. Rev.* 2023, *10*, nwac172.
(25) Luo, Y.; Wang, M.; Wan, C.; Cai, P.; Loh, X. J.; Chen, X. Devising Materials Manufacturing Toward Lab-to-Fab Translation of Flexible Electronics. *Adv. Mater.* 2020, *32*, No. e2001903.
(26) Yu, Y.; Nyein, H. Y. Y.; Gao, W.; Javey, A. Flexible Electrochemical Bioelectronics: The Rise of In Situ Bioanalysis. *Adv. Mater.* 2020, *32*, No. e1902083.
(27) Jeong, W.; Song, J.; Bae, J.; Nandanapalli, K. R.; Lee, S. Breathable Nanomesh Humidity Sensor for Real-Time Skin Humidity Monitoring. *ACS Appl. Mater. Interfaces* 2019, *11*, 44758−44763.
(28) Kano, S.; Kim, K.; Fujii, M. Fast-Response and Flexible Nanocrystal-Based Humidity Sensor for Monitoring Human Respiration and Water Evaporation on Skin. *ACS Sens.* 2017, *2*, 828−833.
(29) Dai, J.; Zhao, H.; Lin, X.; Liu, S.; Liu, Y.; Liu, X.; Fei, T.; Zhang, T. Ultrafast Response Polyelectrolyte Humidity Sensor for Respiration Monitoring. *ACS Appl. Mater. Interfaces* 2019, *11*, 6483−6490.
(30) Cho, M. Y.; Kim, I. S.; Kim, S. H.; Park, C.; Kim, N. Y.; Kim, S. W.; Kim, S.; Oh, J. M. Unique Noncontact Monitoring of Human Respiration and Sweat Evaporation Using a $CsPb_2Br_5$-Based Sensor. *ACS Appl. Mater. Interfaces* 2021, *13*, 5602−5613.
(31) Mondal, S.; Kim, S. J.; Choi, C. G. Honeycomb-like MoS_2 Nanotube Array-Based Wearable Sensors for Noninvasive Detection of Human Skin Moisture. *ACS Appl. Mater. Interfaces* 2020, *12*, 17029−17038.
(32) Duan, Z.; Jiang, Y.; Tai, H. Recent advances in humidity sensors for human body related humidity detection. *J. Mater. Chem. C* 2021, *9*, 14963−14980.
(33) Liu, L. X.; Chen, W.; Zhang, H. B.; Wang, Q. W.; Guan, F.; Yu, Z. Z. Flexible and Multifunctional Silk Textiles with Biomimetic Leaf-Like MXene/Silver Nanowire Nanostructures for Electromagnetic Interference Shielding, Humidity Monitoring, and Self-Derived Hydrophobicity. *Adv. Funct. Mater.* 2019, *29*, 1905197.
(34) Wang, X.; Liu, Y.; Cheng, H.; Ouyang, X. Surface Wettability for Skin-Interfaced Sensors and Devices. *Adv. Funct. Mater.* 2022, *32*, 2200260.
(35) Pei, Y.; Zhang, X.; Hui, Z.; Zhou, J.; Huang, X.; Sun, G.; Huang, W. $Ti_3C_2T_x$ MXene for Sensing Applications: Recent Progress, Design Principles, and Future Perspectives. *ACS Nano* 2021, *15*, 3996−4017.
(36) An, H.; Habib, T.; Shah, S.; Gao, H.; Patel, A.; Echols, I.; Zhao, X.; Radovic, M.; Green, M. J.; Lutkenhaus, J. L. Water Sorption in MXene/Polyelectrolyte Multilayers for Ultrafast Humidity Sensing. *ACS Appl. Nano Mater.* 2019, *2*, 948−955.
(37) Li, X.; Lu, Y.; Shi, Z.; Liu, G.; Xu, G.; An, Z.; Xing, H.; Chen, Q.; Han, R. P. S.; Liu, Q. Onion-inspired MXene/chitosan-quercetin multilayers: Enhanced response to H_2O molecules for wearable human physiological monitoring. *Sens. Actuators B* 2021, *329*, 129209.
(38) Fan, M.; Xia, X.; Li, S.; Zhang, R.; Wu, L.; Qu, M.; Tang, P.; Bin, Y. Sustainable bacterial cellulose reinforced carbon nanotube buckypaper and its multifunctionality for electromagnetic interference shielding, Joule heating and humidity sensing. *Chem. Eng. J.* 2022, *441*, 136103.
(39) Ray, T. R.; Ivanovic, M.; Curtis, P. M.; Franklin, D.; Guventurk, K.; Jeang, W. J.; Chafetz, J.; Gaertner, H.; Young, G.; Rebollo, S.; Model, J. B.; Lee, S. P.; Ciraldo, J.; Reeder, J. T.; Hourlier-Fargette, A.; Bandodkar, A. J.; Choi, J.; Aranyosi, A. J.; Ghaffari, R.; McColley, S. A.; Haymond, S.; Rogers, J. A. Soft, skin-interfaced sweat stickers for cystic fibrosis diagnosis and management. *Sci. Transl. Med.* 2021, *13*, eabd8109.
(40) Liu, Y.; Sheng, Z.; Huang, J.; Liu, W.; Ding, H.; Peng, J.; Zhong, B.; Sun, Y.; Ouyang, X.; Cheng, H.; Wang, X. Moisture-resistant MXene-sodium alginate sponges with sustained superhydrophobicity for monitoring human activities. *Chem. Eng. J.* 2022, *432*, 134370.
(41) Chen, W. Y.; Lai, S. N.; Yen, C.-C.; Jiang, X.; Peroulis, D.; Stanciu, L. A. Surface Functionalization of $Ti_3C_2T_x$ MXene with Highly Reliable Superhydrophobic Protection for Volatile Organic Compounds Sensing. *ACS Nano* 2020, *14*, 11490−11501.
(42) Liu, M.; Guo, T. Preparation and swelling properties of crosslinked sodium polyacrylate. *J. Appl. Polym. Sci.* 2001, *82*, 1515−1520.

https://doi.org/10.1021/acsnano.2c11267
ACS Nano 2023, 17, 5588−5599

(43) Yang, Z.; Liu, A.; Wang, C.; Liu, F.; He, J.; Li, S.; Wang, J.; You, R.; Yan, X.; Sun, P.; Duan, Y.; Lu, G. Improvement of Gas and Humidity Sensing Properties of Organ-like MXene by Alkaline Treatment. *ACS Sens.* 2019, *4*, 1261−1269.
(44) Smith, A. D.; Elgammal, K.; Niklaus, F.; Delin, A.; Fischer, A. C.; Vaziri, S.; Forsberg, F.; Rasander, M.; Hugosson, H.; Bergqvist, L.; Schroder, S.; Kataria, S.; Ostling, M.; Lemme, M. C. Resistive graphene humidity sensors with rapid and direct electrical readout. *Nanoscale* 2015, *7*, 19099−109.
(45) Ali, S.; Hassan, A.; Hassan, G.; Bae, J.; Lee, C. H. All-printed humidity sensor based on graphene/methyl-red composite with high sensitivity. *Carbon* 2016, *105*, 23−32.
(46) Park, S. Y.; Lee, J. E.; Kim, Y. H.; Kim, J. J.; Shim, Y. S.; Kim, S. Y.; Lee, M. H.; Jang, H. W. Room temperature humidity sensors based on rGO/MoS_2 hybrid composites synthesized by hydrothermal method. *Sens. Actuators B* 2018, *258*, 775−782.
(47) Chen, C.; Wang, X.; Li, M.; Fan, Y.; Sun, R. Humidity sensor based on reduced graphene oxide/lignosulfonate composite thin-film. *Sens. Actuators B* 2018, *255*, 1569−1576.
(48) Shanmugam, G.; Deshpande, U. P.; Sharma, A.; Shirage, P. M.; Bhobe, P. A. Impact of Different Morphological Structures on Physical Properties of Nanostructured SnSe. *J. Phys. Chem. C* 2018, *122*, 13182−13192.
(49) Choi, S. J.; Yu, H.; Jang, J. S.; Kim, M. H.; Kim, S. J.; Jeong, H. S.; Kim, I. D. Nitrogen-Doped Single Graphene Fiber with Platinum Water Dissociation Catalyst for Wearable Humidity Sensor. *Small* 2018, *14*, No. e1703934.
(50) Trung, T. Q.; Duy, L. T.; Ramasundaram, S.; Lee, N. E. Transparent, stretchable, and rapid-response humidity sensor for body-attachable wearable electronics. *Nano Res.* 2017, *10*, 2021−2033.
(51) Pawbake, A. S.; Jadkar, S. R.; Late, D. J. High performance humidity sensor and photodetector based on SnSe nanorods. *Mater. Res. Express* 2016, *3*, 105038.
(52) Zhang, D.; Tong, J.; Xia, B. Humidity-sensing properties of chemically reduced graphene oxide/polymer nanocomposite film sensor based on layer-by-layer nano self-assembly. *Sens. Actuators B* 2014, *197*, 66−72.
(53) Li, T.; Li, L.; Sun, H.; Xu, Y.; Wang, X.; Luo, H.; Liu, Z.; Zhang, T. Porous Ionic Membrane Based Flexible Humidity Sensor and its Multifunctional Applications. *Adv. Sci.* 2017, *4*, 1600404.
(54) Fu, T.; Zhu, J.; Zhuo, M.; Guan, B.; Li, J.; Xu, Z.; Li, Q. Humidity sensors based on graphene/SnO_x/CF nanocomposites. *J. Mater. Chem. C* 2014, *2*, 4861−4866.
(55) Pang, Y.; Jian, J.; Tu, T.; Yang, Z.; Ling, J.; Li, Y.; Wang, X.; Qiao, Y.; Tian, H.; Yang, Y.; Ren, T. L. Wearable humidity sensor based on porous graphene network for respiration monitoring. *Biosens. Bioelectron* 2018, *116*, 123−129.
(56) Hu, X.; Gong, J.; Zhang, L.; Yu, J. C. Continuous Size Tuning of Monodisperse ZnO Colloidal Nanocrystal Clusters by a Microwave-Polyol Process and Their Application for Humidity Sensing. *Adv. Mater.* 2008, *20*, 4845−4850.
(57) Wang, X.; Xiong, Z.; Liu, Z.; Zhang, T. Exfoliation at the liquid/air interface to assemble reduced graphene oxide ultrathin films for a flexible noncontact sensing device. *Adv. Mater.* 2015, *27*, 1370−5.
(58) Khandare, L.; Terdale, S. S.; Late, D. J. Ultra-fast α-MoO_3 nanorod-based Humidity sensor. *Adv. Device Mater.* 2016, *2*, 15−22.
(59) Kwak, S. S.; Yoo, S.; Avila, R.; Chung, H. U.; Jeong, H.; Liu, C.; Vogl, J. L.; Kim, J.; Yoon, H. J.; Park, Y.; Ryu, H.; Lee, G.; Kim, J.; Koo, J.; Oh, Y. S.; Kim, S.; Xu, S.; Zhao, Z.; Xie, Z.; Huang, Y.; Rogers, J. A. Skin-Integrated Devices with Soft, Holey Architectures for Wireless Physiological Monitoring, With Applications in the Neonatal Intensive Care Unit. *Adv. Mater.* 2021, *33*, No. e2103974.
(60) Taylor, N. A.; Machado-Moreira, C. A. Regional variations in transepidermal water loss, eccrine sweat gland density, sweat secretion rates and electrolyte composition in resting and exercising humans. *Extrem. Physiol. Med.* 2013, *2*, 4.
(61) Wan, Z.; Liu, Y.; Chen, S.; Song, K.; Peng, Y.; Zhao, N.; Ouyang, X.; Wang, X. Facile fabrication of a highly durable and flexible MoS_2@RTV sponge for efficient oil-water separation. *Colloids Surf., A* 2018, *546*, 237−243.
(62) Chen, J.; Yuan, L.; Shi, C.; Wu, C.; Long, Z.; Qiao, H.; Wang, K.; Fan, Q. H. Nature-Inspired Hierarchical Protrusion Structure Construction for Washable and Wear-Resistant Superhydrophobic Textiles with Self-Cleaning Ability. *ACS Appl. Mater. Interfaces* 2021, *13*, 18142−18151.
(63) Salvo, P.; Pingitore, A.; Barbini, A.; Di Francesco, F. A wearable sweat rate sensor to monitor the athletes' performance during training. *Sci. Sports* 2018, *33*, e51−e58.
(64) Sim, J. K.; Yoon, S.; Cho, Y.-H. Wearable sweat rate sensors for human thermal comfort monitoring. *Sci. Rep.* 2018, *8*, 1−11.
(65) Mondal, S.; Kim, S. J.; Choi, C.-G. Honeycomb-like MoS_2 nanotube array-based wearable sensors for noninvasive detection of human skin moisture. *ACS Appl. Mater. Interfaces* 2020, *12*, 17029−17038.
(66) Zhong, Y.; Huang, S.; Feng, Z.; Fu, Y.; Mo, A. Recent advances and trends in the applications of MXene nanomaterials for tissue engineering and regeneration. *J. Biomed. Mater. Res., Part A* 2022, *110*, 1840−1859.
(67) Nethi, S. K.; Das, S.; Patra, C. R.; Mukherjee, S. Recent advances in inorganic nanomaterials for wound-healing applications. *Biomater. Sci.* 2019, *7*, 2652−2674.
(68) Madhvapathy, S. R.; Wang, H.; Kong, J.; Zhang, M.; Lee, J. Y.; Park, J. B.; Jang, H.; Xie, Z.; Cao, J.; Avila, R.; Wei, C.; D'Angelo, V.; Zhu, J.; Chung, H. U.; Coughlin, S.; Patel, M.; Winograd, J.; Lim, J.; Banks, A.; Xu, S.; Huang, Y.; Rogers, J. A. Reliable, low-cost, fully integrated hydration sensors for monitoring and diagnosis of inflammatory skin diseases in any environment. *Sci. Adv.* 2020, *6*, eabd7146.
(69) Banerjee, M. R. Transient changes in sweating activity of man following ingestion of walter at different temperatures. *Int. J. Biometeorol.* 1970, *14*, 381−390.
(70) Wilke, K.; Martin, A.; Terstegen, L.; Biel, S. S. A short history of sweat gland biology. *Inter. J. Cosmet. Sci.* 2007, *29*, 169−179.
(71) He, J.; Xiao, P.; Shi, J.; Liang, Y.; Lu, W.; Chen, Y.; Wang, W.; Théato, P.; Kuo, S.-W.; Chen, T. High Performance Humidity Fluctuation Sensor for Wearable Devices via a Bioinspired Atomic-Precise Tunable Graphene-Polymer Heterogeneous Sensing Junction. *Chem. Mater.* 2018, *30*, 4343−4354.
(72) Wang, W.; Nayeem, M. O. G.; Wang, H.; Wang, C.; Kim, J. J.; Wang, B.; Lee, S.; Yokota, T.; Someya, T. Gas-Permeable Highly Sensitive Nanomesh Humidity Sensor for Continuous Measurement of Skin Humidity. *Adv. Mater. Technol.* 2022, *7*, 2200479.

https://doi.org/10.1021/acsnano.2c11267
ACS Nano 2023, 17, 5588−5599